

NMF in LM

Introduction

Localisation microscopy (LM) is a conceptually simple and accessible technique providing super-resolution fluorescent images.^{7,9,11,15} The structure of the sample is reconstructed by localising individual fluorophores with precision surpassing¹⁶ the classical resolution limit. $\delta = 0.61 \frac{\lambda}{NA}$, where λ is the wavelength of the emission light and NA is the numerical aperture of the objective lens. LM makes use of the fluorophore transition between bright (ON) and dark (OFF) states to discriminate individual sources separated by a distance $d < \delta$. Super-resolution is achieved by a repetitive localisation of the different individual spatially separated subsets of fluorophores. The number of ON sources in each acquisition frame must be optimised experimentally.¹⁹ A high density of the ON fluorophores results in overlapping sources and complicates localisation whereas a small density leads to a long acquisition time. Standard LM techniques (fPALM,⁷ STORM¹⁸) control the density of the ON sources by photo-switching. However, some recent research suggests algorithms which can deal with a high density of ON sources.⁸

Quantum dots (QD) are an order of magnitude brighter compared to the organic dyes used in conventional LM.^{10,17} Under continuous excitation the QDs exhibit a stochastic blinking between ON and OFF states.²⁰ Excellent photo-stability, low cyto-toxicity and distinctive spectral properties make QDs very attractive for biological research.¹⁷ However, the stochastic blinking of QDs is impractical for standard LM because the rate of ON-OFF transitions and hence the density of ON sources is difficult to control. QD labeled data typically consist of highly overlapping sources which cannot be localised with standard LM techniques.

Methods

We used non-negative matrix factorisation (NMF)¹² as a natural model for QD data. NMF decomposes a movie of the blinking QDs into spatial and temporal parts (i.e. time independent emission profiles of the individual sources and fluctuating intensities of each emitter, respectively). NMF imposes natural non-negativity constraints on both the spatial and the temporal components. Moreover, we used the NMF algorithm¹³ which maximises the likelihood of the model for data corrupted with Poisson noise.

NMF does not put any additional constraints on the shape (point spread function PSF) or blinking behaviour of the individual sources, apart from being non-negative. Therefore NMF can separate overlapping sources of differing shapes and blinking characteristics. Variability in PSFs can, for example, arise in a 3D sample where fluorophores can be in different focal depths and therefore each exhibiting a unique PSF.

Some methods exploiting the blinking behaviour of the QDs have been proposed. Independent component analysis (ICA) of the QD data¹⁴ is a factorisation method with different set of constraints compared to NMF. The separated components are required to be statistically independent, rather than non-negative. ICA allows negative entries and does not account for noise in the measured data which can make recovery of the individual sources difficult from a realistic noisy data (see fig.A.2 in supplementary materials). Maximum a-posteriori (MAP) fitting of the positions and the intensities of known point spread functions (PSFs) to blinking QDs⁶ has been demonstrated. This method, however, requires a prior knowledge about the PSF shape and assumes the PSF to be identical for all emitters. Higher order statistic analysis of the intensity fluctuation (SOFI)⁵ can provide resolution improvement. The intensity of the sources in the SOFI image, however, reflects the fluctuation behaviour rather than the strength of the emitter.⁴ Sources which do not show a fluctuation in the intensity will not appear in the SOFI image. Note that NMF can separate a static source from the fluctuating one and the intensity of the sources can be determined from the temporal part.

Model comparison

The NMF algorithm requires prior knowledge about the number of sources K to be separated. Principal component analysis of the data (PCA) can be used as a simple method for dimensionality estimation. However, for noisy data the estimation of K is difficult.

The results of NMF are the maximum-likelihood estimates, and therefore a higher K leads to a higher likelihood (or a lower residual error) as more sources are better able to fit the data. However, overestimating K produces spurious sources. On the other hand, underestimation of K results in incorrect source shapes as one component must fit several sources. Therefore a reliable estimation of K is vital for a successful separation.

Bayesian treatment of the probabilistic NMF formu-

lation (Gamma - Poisson (GaP) model)³ can quantify evidence of particular K for given data. We showed on simulated data that variational approximation of the GaP model² systematically underestimates the values of K (see supplementary materials for details).

An alternative approach is to analyse the residuals (difference between data and estimated model) for models with different K . Models with low K give rise to correlations in residuals because multiple individual emitters have to be represented with fewer components. Correlations decrease with higher K . We selected the smallest K which reduces the residual correlations to a level where further increase of the K do not decrease the correlations any further. Simulations suggest that this approach can provide most reliable estimation of K compared to PCA and variational GaP. (Details in supplementary materials.)

Results

Tests on simulated data with different densities of ten QDs suggests (see supplementary materials) that the analysis of the residuals in correlations provides the most accurate estimate of the number of sources K . We used this method in further computations.

Simulations of noisy data comprising two QDs show that NMF can reliably separate two close emitters ($d > \delta/10$) when K_{true} is known ($K = K_{\text{true}}$). However, the ability to estimate K correctly becomes increasingly difficult for closely spaced sources. The high correlations in residuals for $K < K_{\text{true}}$ arise only when the two sources are separated by at least $d > \delta/5$, where $\delta = 0.61\lambda/\text{NA}$ is the classical resolution limit (fig. A.1).

Out of focus PSF

NMF can extract individual sources with differing shape because apart from the non-negativity there are no further constraints on the separated components. We show a separation of overlapping out-of-focus point spread functions (PSF) from a movie (10^3 frames) of several blinking QDs (fig. A.5). Individual emitters were in slightly different focal depths and therefore each QD produced a distinctive PSF. As can be seen from fig.A.5 individual PSFs were highly overlapping in each frame.

The number of components was estimated from the analysis of the correlations in residual (fig.A.6). NMF

was able to recover images of individual sources which correspond to realistic out-of-focus PSFs (fig. A.5). It also recovered sources with PSFs only partially present in the selected region.

Discussion

We have demonstrated that NMF allows to separate individual emitters from a movie of blinking QDs. The ability to recover PSFs with different shapes from the data with highly overlapping sources makes the method attractive for imaging of 3D samples where fluorophores can be in different focal depths and therefore produce a variety of different PSFs. Diversity in PSFs for individual sources can also arise with aberrations in the optical system.

Reliable estimation of the number of sources is important for correct recovery of individual components. This is a difficult task for data with a high density of overlapping sources. We demonstrated on simulated data the limitations this imposes on resolution of the method.

NMF allows localisation microscopy with blinking QDs, however, NMF is not limited to QDs only. It can separate any source with intermittent intensity as long as the actual fluorophores remain static in space during the acquisition period. A typical data set consists of 10^3 frames and therefore the acquisition time is typically in order of tens of seconds. During this period the sample must remain still. This is a common limiting factor for localisation microscopy techniques. However, as NMF can separate overlapping sources it can speed up the acquisition compared to the standard LM techniques.¹⁹ Moreover the possibility of using QDs can make the exposure time shorter because QDs are usually brighter than common organic fluorophores used in LM.

NMF does not take into account the temporal structure of the data. Time frames can be permuted without affecting the separated components. However, there is a clear temporal structure in QDs blinking - the periods of ON and OFF times. Exploiting this information would likely facilitate the factorisation and will be a subject to further research.

Acknowledgements

We would like to thank to Rory Duncan and Colin Rickman for their help with QD data acquisition.

A Supplementary materials

Real samples

A solution of QDs (Qdot 565, invitrogen) was deposited and dried on a coverslip and imaged with a standard wide-field microscope (100x, 1.4NA) on a CCD camera (64nm pixel-size). We acquired 10^3 frames each with 100 ms exposure time. The total acquisition time was about 2 mins.

The camera pixels values were converted into a photon counts with a gain estimated from a calibration measurement.

Simulated data

The parameters used for simulations are shown in table A.1. The individual QDs were generated as in-focus point-spread functions and the intensity of each source was generated from uniform distribution on the interval $[0, I_{max}]$. A uniform constant background was added to each frame and all pixels were corrupted with Poisson noise.

We generated two different collections of data-sets. In the first collection we simulated two sources ($K_{\text{true}} = 2$) separated by a distance $d = 0.1$ to 1.2 pixels. In the second collection we simulated ten sources ($K_{\text{true}} = 10$) distributed within a circular area with diameter $r = \delta, 1.5\delta$ and 2δ , where $\delta = 0.61 \frac{\lambda}{\text{NA}}$ is the classical resolution limit. Position of the sources were chosen at random while keeping the distance between any two sources at least δ/K_{true} to avoid clustering. Each dataset in both collections was generated 10 times with a random geometric configuration of the individual sources.

NMF model of the blinking QDs

A movie of blinking quantum dots can be regarded as an $N \times T$ data matrix \mathbf{D} where N is the number of pixels and T is the number of time frames in the movie. Each frame in the movie is transformed into a column of the matrix \mathbf{D} by concatenating columns of the 2D image into a $N \times 1$ vector. Non-negative matrix factorisation (NMF) makes an approximative decomposition

$$\mathbf{D} \approx \mathbf{W}\mathbf{H}, \quad (\text{A.1})$$

where the $N \times T$ matrix \mathbf{D} is expressed as a multiplication of the $N \times K$ matrix \mathbf{W} and $K \times T$ matrix \mathbf{H} , subject to non-negativity constraints on the entries $w_{nk} \geq 0$ and $h_{kt} \geq 0$. Each column \mathbf{w}_k of the matrix \mathbf{W} (a $N \times 1$ vector) then represents an image of the k th source and each row \mathbf{h}_k of the matrix \mathbf{H} ($1 \times T$ vector) represents the time profile of the k th source intensity.

The NMF algorithm¹³ makes the decomposition (A.1) such that the likelihood function of the model is maximised under assumption of Poisson noise. The approximative factorisation (A.1) can then be written as

$$\mathbb{E}[\mathbf{D}] = \mathbf{W}\mathbf{H}, \quad (\text{A.2})$$

where $\mathbb{E}[\cdot]$ denotes expectation value of the noisy data with respect to the Poisson distribution.

NMF updates

We used iterative NMF updates¹³ to compute the factorisation (A.2)

$$\begin{aligned} w_{nk} &= \frac{w_{nk}}{\sum_{t=1}^T h_{kt}} [(\mathbf{D}./\mathbf{W}\mathbf{H})\mathbf{H}^\top]_{nk} \\ h_{kt} &= \frac{h_{kt}}{\sum_{n=1}^N w_{nk}} [\mathbf{W}^\top(\mathbf{D}./\mathbf{W}\mathbf{H})]_{kt} \end{aligned} \quad (\text{A.3})$$

where the ‘./’ operation refers to an element-wise division. The matrix elements w_{nk} and h_{kt} were initialised at random from the uniform distribution. The columns of the matrix \mathbf{W} were normalised such that $\sum_n w_{nk} = 1$ and therefore the entries h_{kt} correspond to a number of photons emitted from the source k at time t . One component was added as a homogeneous, static background: $w_{n(K+1)} = \frac{1}{N}$, $h_{(K+1)t} = Nb$, where the background value b was estimated from the dark regions of the data averaged over time $\frac{1}{T} \sum_t d_{nt}$. This component was not updated over the iterations. We run each NMF evaluation with five partial restarts - after each run converges we restarted the values of w_{nk} and run the updates for both \mathbf{W} and \mathbf{H} again. The new result is accepted if the likelihood function increases. This procedure helps to reach a better local minimum.

Comparison to ICA

Comparison of NMF and ICA separated components from simulated data of two QDs is shown in fig.A.2. ICA can separate components from noise-free data (fig.A.2c), however fails in the noisy case (fig.A.2b). Our NMF model accounts for Poisson noise and is able to separate the sources even from noisy data (fig.A.2a).

Gamma-Poisson model

The gamma-Poisson (GaP) model has been proposed as a probabilistic model for NMF.³ The entries h_{kt} of the intensity matrix \mathbf{H} are regarded as latent variables generated from a Gamma distribution with parameters α_k, β_k

and the data are modelled as a Poisson variable with mean \mathbf{WH} as in (A.2). Variables $\theta = \{\mathbf{w}_k, \alpha_k, \beta_k, k = 1..K\}$ are then parameters of the GaP model.

The posterior distribution can be written as $p(K|\mathbf{D}) \propto p(\mathbf{D}|K)p(K)$ where $p(K)$ is a prior distribution over values of K . If we assume the prior $p(K)$ to be equal for each K , we can express $p(K|\mathbf{D}) \propto p(\mathbf{D}|K)$ where the marginal likelihood $p(\mathbf{D}|K) = \int p(\mathbf{D}|K, \theta)p(\theta|K)d\theta$ requires integration over the parameters θ . The variational approximation of the GaP model² provides a lower bound \mathcal{L} on the likelihood function $p(\mathbf{D}|K, \theta)$ with latent variables \mathbf{h}_k integrated out. The maximum of the lower bound \mathcal{L} computed for different values of K (fig.A.3g-i) can suggest K which maximises $p(\mathbf{D}|K, \theta)$. However, integration over the parameters $p(\mathbf{D}|K) = \int p(\mathbf{D}|K, \theta)p(\theta|K)d\theta$ will penalise the complexity of the model (similar to Bayesian Information Criterion¹) and therefore shift the maximum of $p(\mathbf{D}|K)$ towards smaller values of K compared to $p(\mathbf{D}|K, \theta)$. As we show in fig.A.3g-i the lower bound already underestimates the value of K and we can expect that $p(\mathbf{D}|K)$ peaks for even lower K and therefore systematically underestimates the number of sources.

Correlations in residuals

The true number of components K_{true} can also be estimated from the $N \times T$ residual matrix \mathbf{S} (entries s_{xt}). After evaluating the model (A.2) for a specific K , we compute a standardised residual matrix with entries

$$s_{nt} = \frac{d_{nt} - \sum_{k=1}^K w_{nk}h_{kt}}{\sqrt{\sum_{k=1}^K w_{nk}h_{kt}}}.$$

The factor $1/\sqrt{\sum_{k=1}^K w_{nk}h_{kt}}$ is applied in order to standardise the residuals (zero mean and unit variance) of Poisson distributed data. We can then compute the $N \times N$ correlation matrix

$$\mathbf{C}_S = \mathbf{S}\mathbf{S}^T,$$

and the $N \times N$ matrix of the correlation coefficients \mathbf{R}_S with entries

$$r_{ij} = \frac{c_{ij}}{\sqrt{c_{ii}c_{jj}}}. \quad (\text{A.4})$$

Underestimation of the number of sources ($K < K_{\text{true}}$) will lead to correlations between some pixels as the model will try to explain multiple sources with one component. For $K \geq K_{\text{true}}$ the correlations are expected to drop to a base level and the residuals become uncorrelated. We can pick up the value of $K = \hat{K}$ for which the residual correlations decrease to a certain level and $K > \hat{K}$ does not give any further improvement. \hat{K} represents a ‘kink’ in the lines fig.A.3(j-l).

Localisation error

To asses the localisation performance of NMF we used dataset of two QDs ($K_{\text{true}} = 2$) separated by d and assumed that the number of sources is known $K = K_{\text{true}}$. Sources were localised as a maximum likelihood fit of an isotropic 2D gaussian with a centre $\hat{\mathbf{x}}_k$ to the separated components \mathbf{w}_k . We computed the mean relative localisation error as

$$\varepsilon = \frac{1}{d} \frac{e_1 + e_2}{2}$$

where $e_k = |\hat{\mathbf{x}}_k - \mathbf{x}_k^{\text{true}}|$ corresponds to the localisation error of the k th source located at $\mathbf{x}_k^{\text{true}}$ and $d = |\mathbf{x}_1^{\text{true}} - \mathbf{x}_2^{\text{true}}|$ is the true separation of the emitters. The estimated ε for different values of d is shown as a magenta line in fig.A.1. For $d > 30$ nm the mean localisation error is less than 20% of the separation d ($\varepsilon = 0.2$) and is further decreasing for higher values of d .

Estimation of K

We compared the performance of the the principal component analysis (PCA), variational approximation of GaP model and the analysis of the residual correlations in K estimation task. We used simulated data comprising 10 sources ($K_{\text{true}} = 10$). The mean image of the data with three different densities of sources is shown in the first line of fig.A.3. We generated data with 10 random geometric configuration for each density. The first 18 principal components (PC) eigenvalues for three different random configurations are plotted in the second row of fig.A.3.

For sparse data (left column) we can estimate the number of components from the ‘kink’ in the spectrum of PC eigenvalues at $K = 10$. However, for dense data (right) this estimation is impossible to make because the PC eigenvalues drop very gradually.

The variational lower bound for models with different K for three different geometric configuration of the sources is plotted in the third line of fig.(A.3). The lower bound peaks at the correct $K = K_{\text{true}}$ for sparse data set (left), but for the denser data (right) it tends to reach the maximum for $K < K_{\text{true}}$. The variational lower bound systematically underestimates the value of K .

The maximum correlation coefficient (A.4) in residuals $\max_{i,j}(r_{ij})$ is shown in the last line of fig.A.3. The model was estimated using the NMF updates(A.3). Values for three different configurations are shown. We can pick the K where the ‘kink’ occurs.

We used an automatic procedure to estimate the ‘kink’ in the graphs for PCA and maximum residual correlations (fig.A.3(d-f) and (j-k), respectively). The data were partitioned into two subsets corresponding to $[K_{\text{min}}..K' - 1]$ and $[K'..K_{\text{max}}]$ where K_{min} and K_{max} is the minimum and the maximum values of K , respectively. We fit a line to each of the subsets. The kink was determined at K' which resulted in a partition with a smallest mean squared error of for the fit of two lines.

A histogram of estimated K for PCA, GaP and the maximum residual correlations is shown in fig.A.4c. The analyses of the maximum residual correlation provides the best better estimate for K .

We used the simulated data of two QDs ($K_{\text{true}} = 2$) separated by $d = 0.1$ to 1.2 pixels to evaluated the model for $K = 1, 2$ and 3 and analysed the residual correlations eq.(A.4). The maximum value $\max_{i,j}(r_{ij})$ in the correlation coefficient matrix (A.4) as a function of d for the three different values of K is shown in fig.A.1(red, green and blue curves). For closely spaced sources ($d \leq 30$ nm) the correlations are approximately on the same level for any K . However, for $d \geq 40$ nm there is a steep increase of the correlations for $K = 1$ (blue line) compared to $K = 2$ (green line). The model with $K = 3$ (red line) does not lead to any further improvement. For this noise level we can therefore estimate the correct $K = 2$ for emitters separated by at least $d > 50$ nm. Comparison with with the localisation error (magenta curve in fig.A.1) shows that the determining factor for resolution of the method is the ability to estimate K correctly (here for $d > 50$ nm).

Tables

Parameter	Value	Description
T	10^3	Number of time slices in the sequence.
K_{true}	10	Number of sources in the simulated data.
b	10^2 photons	Uniform background added to each time slice.
I_{max}	$1.5 \cdot 10^3$ photons	Maximum intensity of a single source in one time slice.
blinking	uniform	Blinking behaviour of the individual sources.
λ_{em}	655 nm	Emission wavelength.
NA	1.2	Numerical aperture of the objective.
pixel-size	106 nm	Size of a pixel in the sample plane.
δ	333 nm (3.1 pixels)	Radius of the region containing the sources ($\delta = 0.61 \frac{\lambda_{\text{em}}}{NA}$).
noise	Poisson	Each pixel was corrupted with Poisson noise.

Table A.1: Parameters of the simulation

Figures

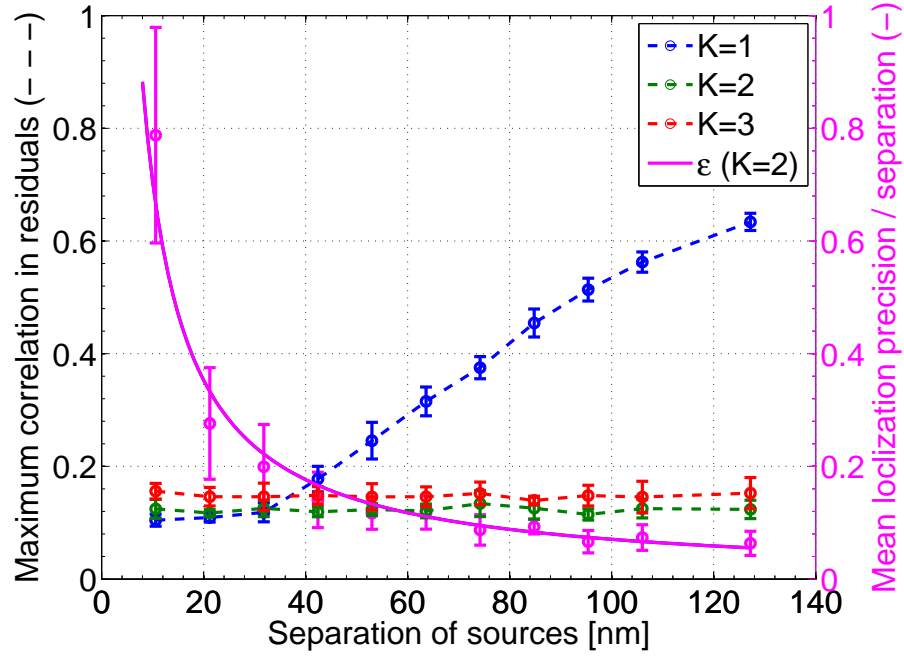


Figure A.1: Simulated data of two sources ($K_{\text{true}} = 2$). The maximum value of correlations in the residuals for $K = 1$ (blue), 2 (green) and 3 (red). Mean localisation error per separation ε for $K = 2$ (magenta) with fitted curve $\propto 1/d$. The differences in residual correlations for $K = 1$ and $K = 2$ are apparent only when the two sources are separated by at least 50 nm. The classical resolution limit is $\delta = 273$ nm.

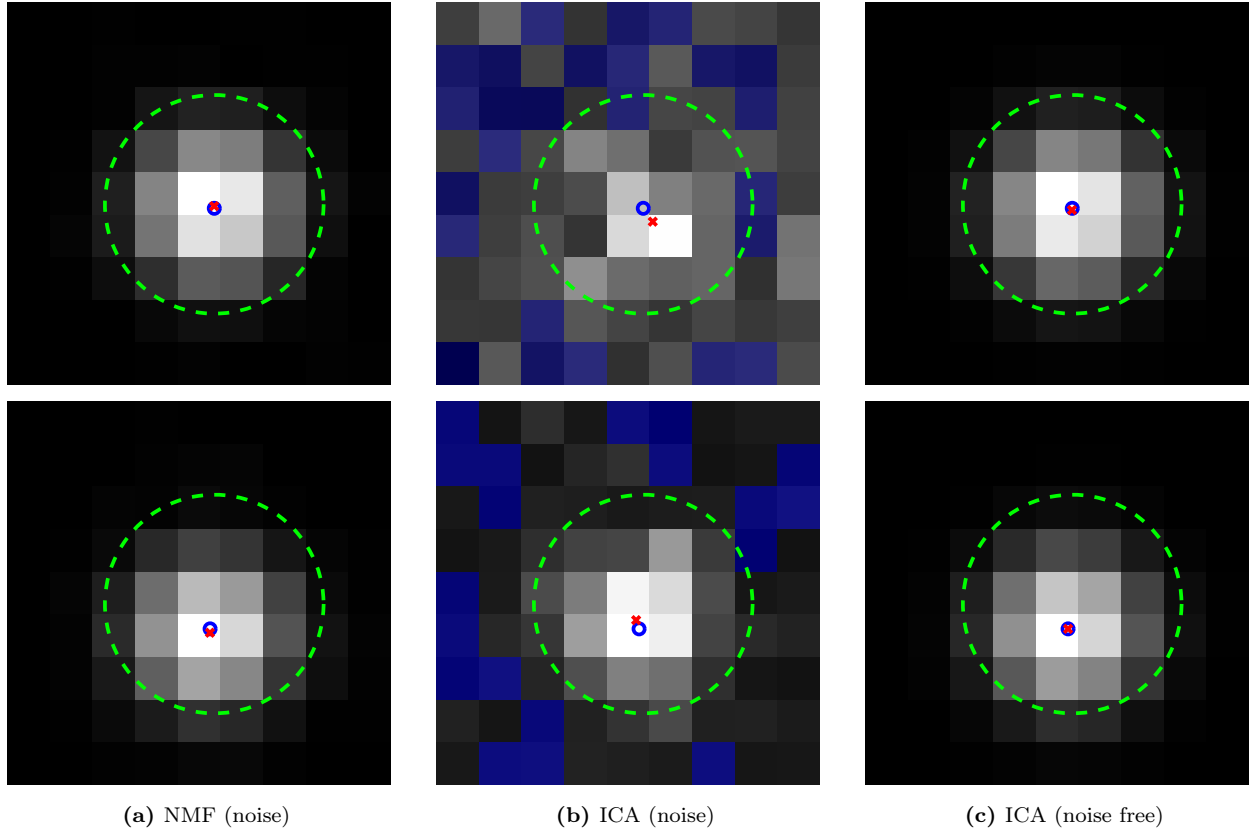


Figure A.2: Comparison of the components separated with NMF (a) and ICA (b) for simulated noisy data of two blinking QDs separated by $d = 50$ nm. Parameters of the simulations are shown in tab.A.1. ICA for noise free data (c). The true and the estimated positions are shown as blue circle and red crosses, respectively. The radius of the green circle is the resolution limit δ . Blue pixels contain negative values.

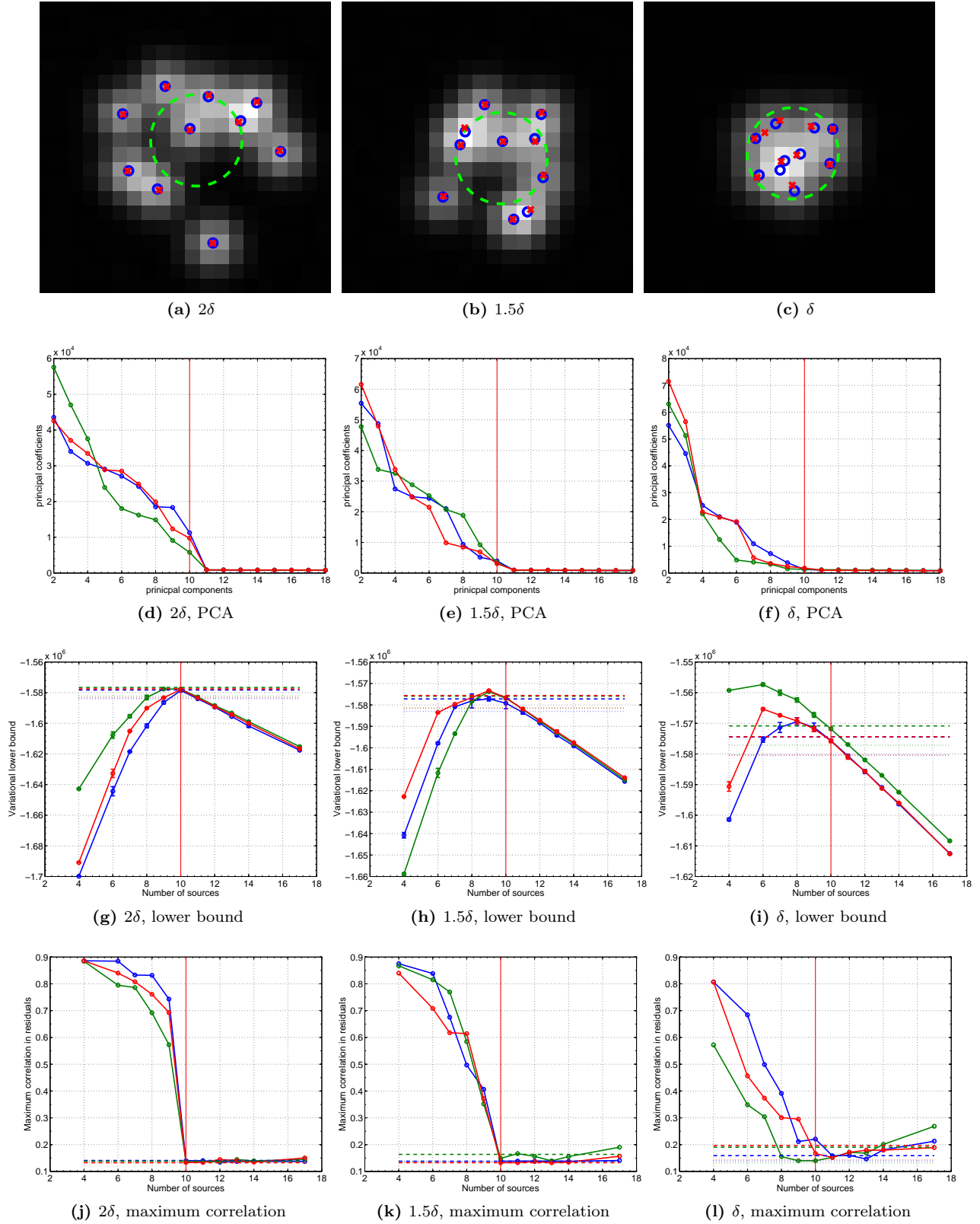


Figure A.3: K estimation for sources contained in a circular area with radius 2δ (left column), 1.5δ (middle column) and δ (right column). Mean (wide field) image of the simulated data (1st row). Blue circles correspond to the true locations of the emitters. Red circles show the estimated locations of the components separated with NMF. Green circle represent an area of the classical resolution limit δ . Principal component analysis (second row), variational lower bound (third row) and maximum residual correlations (bottom row) for corresponding data sets. Red, green and blue curves correspond to three datasets (out of 7) with three different geometric configurations. Dotted lines show the values for \mathbf{W}_{true} and \mathbf{H}_{true} , the values for data generation. Dashed lines show the values when NMF algorithm was initialised with \mathbf{W}_{true} and \mathbf{H}_{true} .

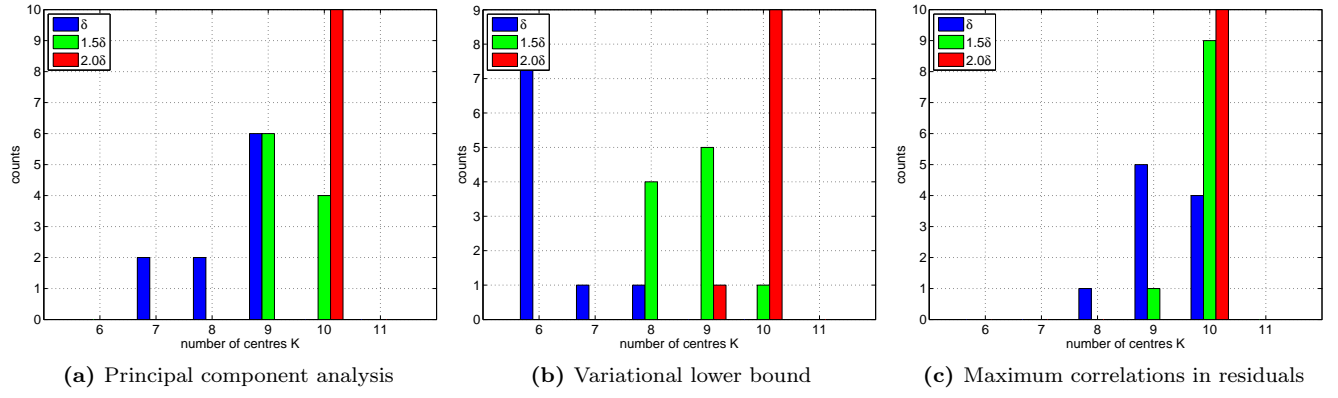


Figure A.4: Histograms of the K estimations for data with three different sources density. ($K_{\text{true}} = 10$)

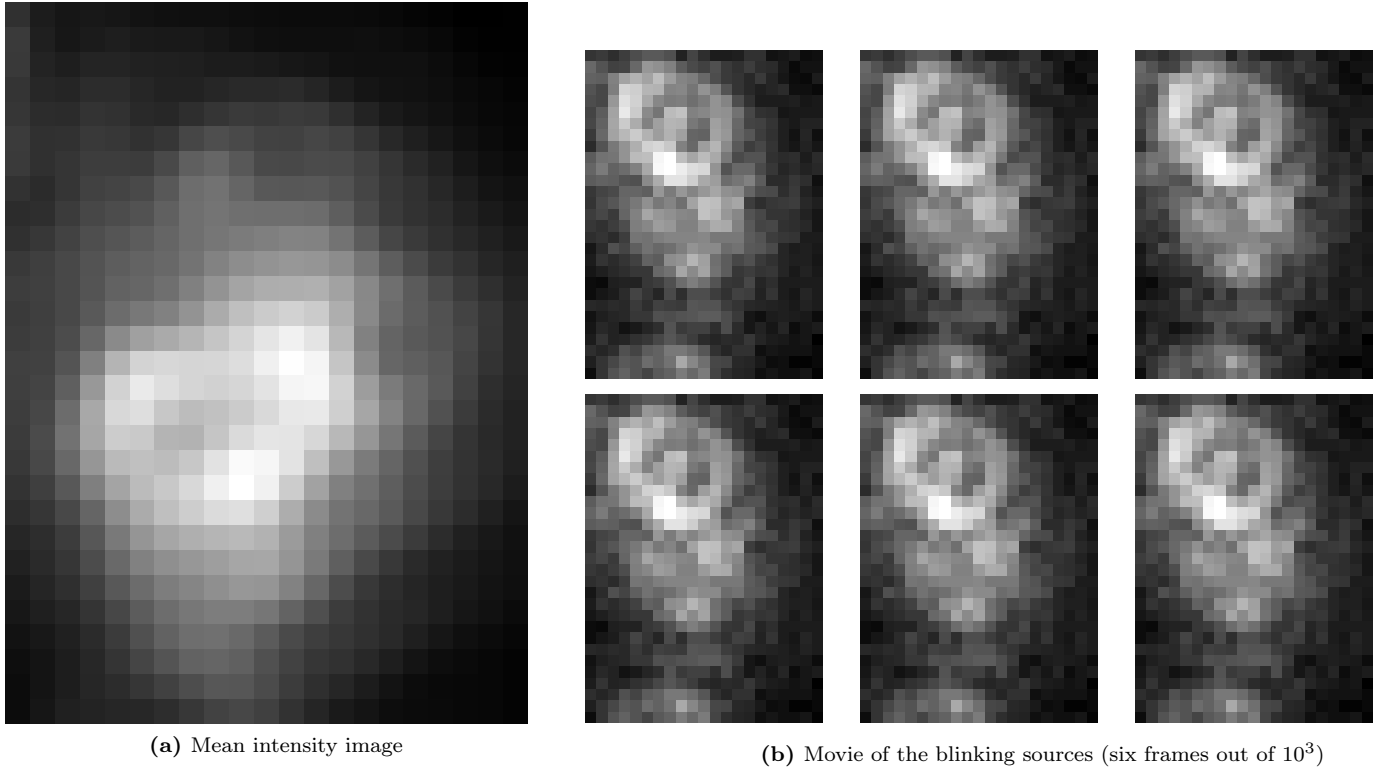


Figure A.5: Real QD data.

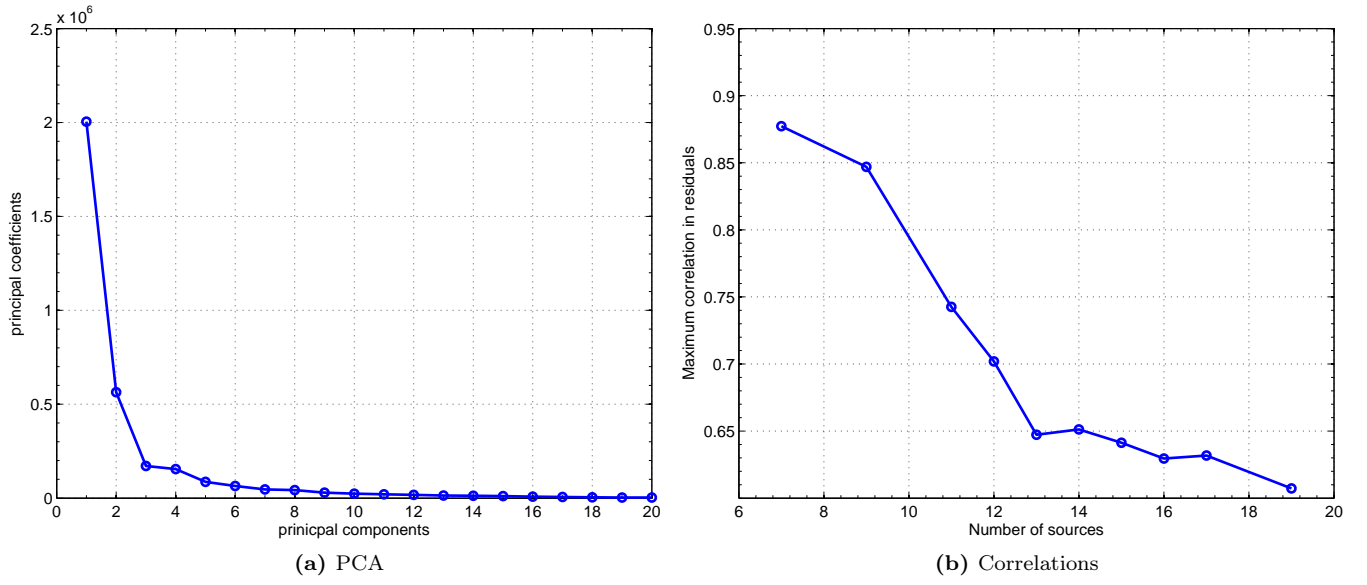


Figure A.6: Estimation of K for the real data - set of out of focus PSFs.

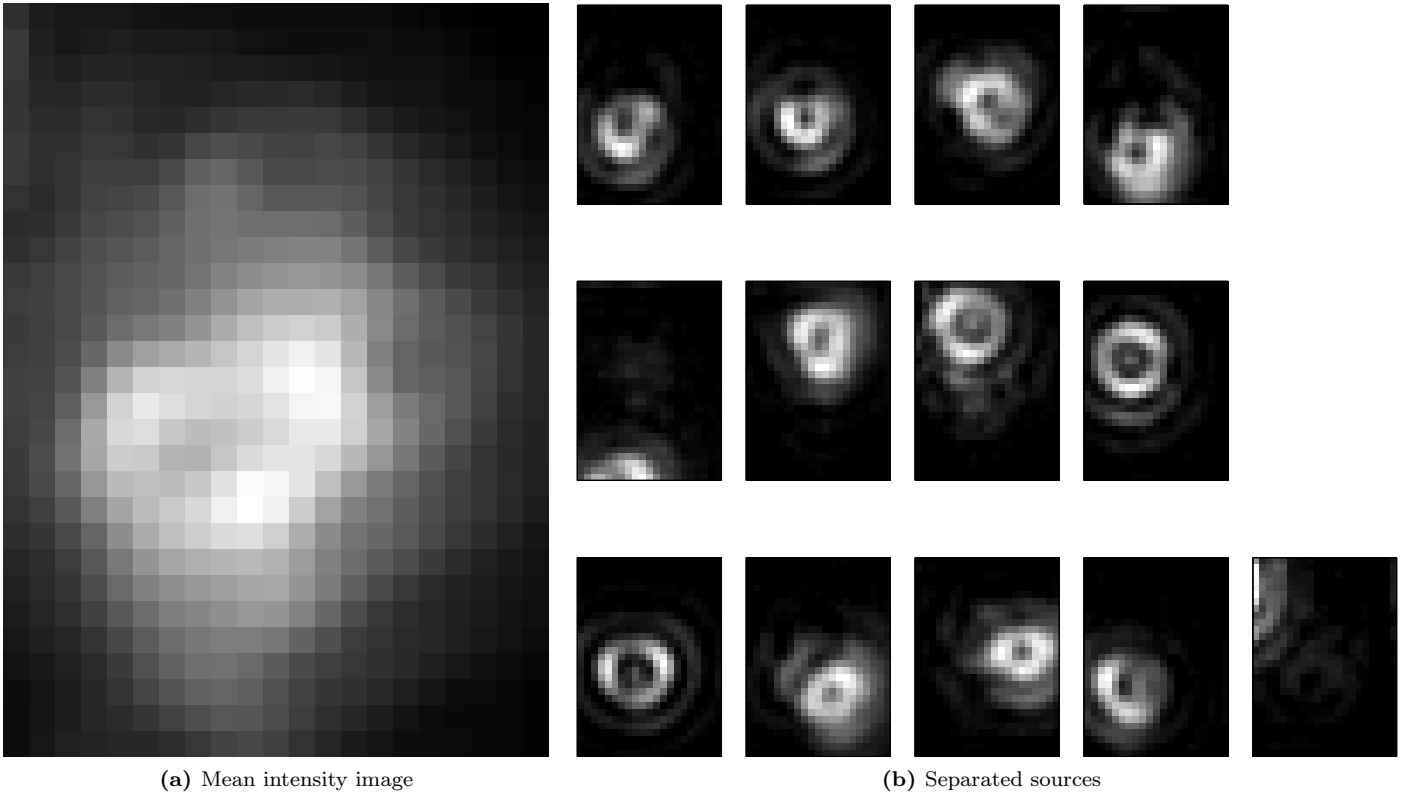


Figure A.7: Left: mean intensity image corresponding to a standard wide-field image. Right: separated individual sources for $K = 13$.

References

- [1] Christopher M. Bishop. *Pattern Recognition and Machine Learning*. Springer, 2006.
- [2] Wray Buntine and Aleks Jakulin. Discrete component analysis. In C. Saunders, M. Grobelnik, S. Gunn, and J. Shawe-Taylor, editors, *Subspace, Latent Structure and Feature Selection*, pages 1–33. Springer, 2006.
- [3] John Canny. GaP: a factor model for discrete data. In *Proceedings of the 27th annual international ACM SIGIR conference on Research and development in information retrieval*, pages 122–129. ACM, 2004.
- [4] T Dertinger, R Colyer, G Iyer, S Weiss, and J Enderlein. Fast, background-free, 3D super-resolution optical fluctuation imaging (SOFI). *Proceedings of the National Academy of Sciences of the United States of America*, 106(52):22287–92, December 2009.
- [5] Thomas Dertinger, Ryan Colyer, Robert Vogel, Jörg Enderlein, and Shimon Weiss. Achieving increased resolution and more pixels with Superresolution Optical Fluctuation Imaging (SOFI). *Optics Express*, 18(18):18875, August 2010.
- [6] Paul Harrington, Jonas Anderson, Bernd Rieger, Diane Lidke, and Keith A Lidke. Poster: A Bayesian Approach to Fluorescence Intermittency Based Localization Microscopy. *Supplement of Biophysical Journal*, 96:20–20, 2008.
- [7] Samuel T Hess, Thanu P K Girirajan, and Michael D Mason. Ultra-high resolution imaging by fluorescence photoactivation localization microscopy. *Biophysical journal*, 91(11):4258–72, December 2006.
- [8] Seamus J Holden, Stephan Uphoff, and Achillefs N Kapanidis. DAOSTORM: an algorithm for high- density super-resolution microscopy. *Nature methods*, 8(4):279–80, April 2011.
- [9] Bo Huang, Wenqin Wang, Mark Bates, and Xiaowei Zhuang. Three-dimensional super-resolution imaging by stochastic optical reconstruction microscopy. *Science (New York, N.Y.)*, 319(5864):810–3, February 2008.
- [10] Jyoti K Jaiswal and Sanford M Simon. Potentials and pitfalls of fluorescent quantum dots for biological imaging. *Trends in cell biology*, 14(9):497–504, September 2004.
- [11] Sara a Jones, Sang-Hee Shim, Jiang He, and Xiaowei Zhuang. Fast, three-dimensional super-resolution imaging of live cells. *Nature methods*, 8(6):499–505, June 2011.
- [12] D D Lee and H S Seung. Learning the parts of objects by non-negative matrix factorization. *Nature*, 401(6755):788–91, October 1999.
- [13] D.D. Lee and H.S. Seung. Algorithms for non-negative matrix factorization. *Advances in neural information processing systems*, 13, 2001.
- [14] Keith A. Lidke, Bernd Rieger, Thomas M. Jovin, and Rainer Heintzmann. Superresolution by localization of quantum dots using blinking statistics. *Optics Express*, 13(18):7052, 2005.
- [15] S. Linde, R. Kasper, M. Heilemann, and M. Sauer. Photoswitching microscopy with standard fluorophores. *Applied Physics B*, 93(4):725–731, October 2008.
- [16] Raimund J Ober, Sripad Ram, and E Sally Ward. Localization accuracy in single-molecule microscopy. *Biophysical journal*, 86(2):1185–200, February 2004.
- [17] Ute Resch-Genger, Markus Grabolle, Sara Cavaliere-Jaricot, Roland Nitschke, and Thomas Nann. Quantum dots versus organic dyes as fluorescent labels. *Nature methods*, 5(9):763–75, September 2008.
- [18] Michael J Rust, Mark Bates, and Xiaowei Zhuang. Sub-diffraction-limit imaging by stochastic optical reconstruction microscopy (STORM). *Nature methods*, 3(10):793–5, October 2006.
- [19] Alexander R Small. Theoretical limits on errors and acquisition rates in localizing switchable fluorophores. *Biophysical journal*, 96(2):L16–8, January 2009.
- [20] Fernando D. Stefani, Jacob P. Hoogenboom, and Eli Barkai. Beyond quantum jumps: Blinking nanoscale light emitters. *Physics Today*, 62(2):34, 2009.